Available online at www.sciencedirect.com
ScienceDirect
Ceramics International 36 (2010) 2137–2145
CERAMICS INTERNATIONAL
www.elsevier.com/locate/ceramint

Spinel precipitation in Sn^{4+}-doped $Co_{1-x}O$ polycrystals with dispersed $Co_{2+x}Sn_{1-x}O_4$ particles

Ching-Yui Pan, Pouyan Shen *

Department of Materials and Optoelectronic Science, National Sun Yat-sen University, Kaohsiung 80424, Taiwan, ROC

Received 15 April 2010; received in revised form 23 April 2010; accepted 3 May 2010
Available online 23 June 2010

Abstract

$Co_{1-x}O$–SnO_2 powders in molar ratio of 92:8 were reactively sintered at 1400 °C to form $Co_{1-x}O$–$Co_{2+x}Sn_{1-x}O_4$ composite and then cooled in furnace or air quenched for secondary $Co_{2+x}Sn_{1-x}O_4$ spinel precipitation from the Sn^{4+} doped $Co_{1-x}O$ grains. Electron microscope observations indicated the secondary spinel to precipitate at grain boundaries when slowly cooled, but as parallel-epitaxial platelets within the Sn^{4+} doped $Co_{1-x}O$ grains with a precipitate free zone near the grain boundary when air quenched. A process of thermal-mismatch induced {1 1 0} cleaving, taking advantage of cobalt vacancies, and spontaneous healing by oxidation precipitation accounts for the platy spinel precipitation within the grains. The precipitate free zone can be attributed to cobalt vacancy depletion, i.e. site saturation, near the grain boundary during rapid cooling in air. The spinel nanocrystals nucleated from cobalt vacancies in association with Sn^{4+} dopant have well-developed {1 1 1} habit plane in order to minimize the coherency strain energy.

Keywords: A. Firing; A. Powders; B. Surfaces; $Co_{1-x}O$

1. Introduction

Defect clustering-induced paracrystal is a typical metastable precipitate for rock salt-type oxide with intrinsic or extrinsic ion dopant and charge- and/or volume-compensating defects assembled in a periodic yet corrugated manner. The paracrystalline distribution is such that the spacing between defects remains fairly constant but the relative lateral translation may be more variable according to theoretical studies of nonstoichiometric wustite, $Fe_{1-x}O$ [1,2]. In fact, $Fe_{1-x}O$ having a considerable degree of nonstoichiometry ($x \leq 0.15$ [3]) was known to possess defect clusters of 4:1 type with 4 octahedral vacant sites surrounding one Fe^{3+}-filled tetrahedral interstitial site [4]. When aged at high temperatures, the 4:1 clusters may assemble into larger units (e.g. 13:4, 16:5 and form a paracrystal [1,2]), which order further into Fe_3O_4 spinel or other ordered phases: p″ and p‴ [5,6]. The experimental results of $Ni_{1-x}O$ dissolved with Zr^{4+} [7] or Ca^{2+} [8], $Co_{1-x}O$ dissolved with Zr^{4+} [9] or Mg^{2+} [10] and CaO dissolved with Ni^{2+} [11] or Co^{2+} [12], further showed that paracrystalline interspacing of defect clusters of rock salt-type oxides could be tailored by doping specific cations.

Recently, rapid cooling of sintered polycrystalline composites was found to cause thermal-mismatch induced {1 1 0} cleaving and spontaneous healing of zirconia dispersed $Co_{1-x}O$ [12]. Polymorphic transformation-induced cleaving and spontaneous healing by precipitation was further experimentally studied in $Co_{1-x}O$ polycrystals containing a dispersion of ZrO_2 particles [13]. In natural occurrence, the oriented rutile needles in garnet from ultra-high pressure eclogites can also be explained by such a cleaving-healing/precipitation process [14].

In this study, $Co_{1-x}O$–$Co_{2+x}Sn_{1-x}O_4$ composite prepared by a reactive sintering route was used to precipitate secondary $Co_{2+x}Sn_{1-x}O_4$ spinel at different nucleation sites from the Sn^{4+}-doped $Co_{1-x}O$ polycrystals upon cooling. We focused on: (1) the precipitation of secondary spinel at grain boundaries when the composite was slowly cooled in the furnace; (2) thermal-mismatch induced {1 1 0}-specific cleaving and spontaneous healing precipitation to form parallel-epitaxial platy spinel within the grains when the composite was rapid cooled in air; and (3) the intrinsic shape of the spinel nucleus in a matrix of rock salt-type proto-oxide, as a comparison with previously reported case of $NiFe_2O_4$ precipitation in NiO [15,16].

* Corresponding author. Tel.: +886 7 5254060; fax: +886 7 5254099.
E-mail address: pshen@mail.nsysu.edu.tw (P. Shen).

0272-8842/$36.00
doi:10.1016/j.ceramint.2010.05.023

2. Material and methods

$Co_{1-x}O$ (Cerac, 99.9%) and SnO_2 (Alfa Aesar, 99.9%) powders in mole ratio of 92:8 (denoted as C92S8) were dry-pressed at 650 MPa into disks 10 mm in diameter and 2 mm in thickness. The pellets were then reactively sintered and homogenized at 1400 °C for up to 200 h followed by cooling in furnace or air quenching to room temperature for precipitation study.

The fired specimens, i.e. $Co_{1-x}O$–$Co_{2+x}Sn_{1-x}O_4$ composites, were analyzed by XRD (Cu Kα, 40 kV, 30 mA, using Siemens D5000 diffractometer) in the 2θ range of 25–80° at a scanning rate of 1°/min (step size 0.05°, fixed counts 3 s) to identify the crystalline phases. The *d*-spacing measured from XRD traces were used for the least-squares refinement of the lattice parameters.

The $Co_{1-x}O$–$Co_{2+x}Sn_{1-x}O_4$ composites were polished with optional thermal etching (100 °C lower than sintering or annealing temperatures) or chemical etching (30% HCl) for scanning electron microscopic (SEM, JEOL JSM-6400, 20 kV) observations coupled with energy dispersive X-ray (EDX) analysis. Secondary electron image (SEI) and back-scattered electron image (BEI) were used to characterize the microstructures of the composites.

Thin sections of the composites were also Ar-ion milled to electron transparency for transmission electron microscopic (TEM, JEOL3010, 300 kV) observations. Bright field image (BFI) and dark field image (DFI) were used to study the microstructures. Selected area electron diffraction (SAED) pattern and lattice image coupled with two-dimensional forward and inverse Fourier transform were used to characterize the secondary spinel precipitates and defect microstructures of the $Co_{1-x}O$–$Co_{2+x}Sn_{1-x}O_4$ composites.

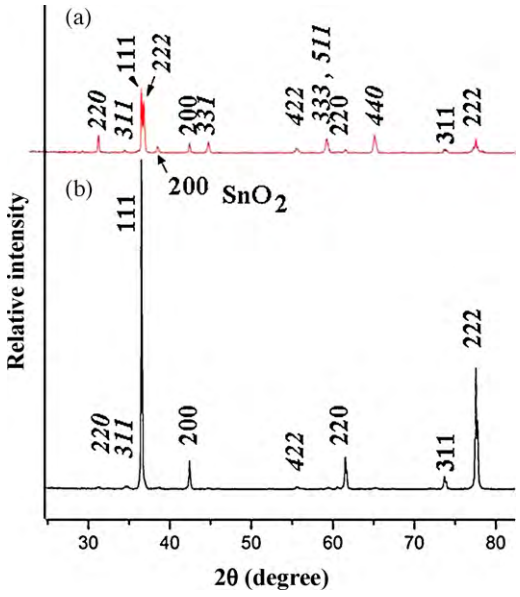

Fig. 1. XRD trace of C92S8 sample reactively sintered at 1400 °C for 24 h and then (a) cooled in furnace, (b) quenched in air showing the diffraction peaks of the predominant phase of Sn^{4+}-doped $Co_{1-x}O$ (denoted by upright *h k l*), minor phase of $Co_{2+x}Sn_{1-x}O_4$ spinel (denoted as italic *h k l*) and relic SnO_2. The different intensity of the spinel phase in (a) and (b) was due to inhomogeneous distribution of the intergranular spinel grains (cf. text).

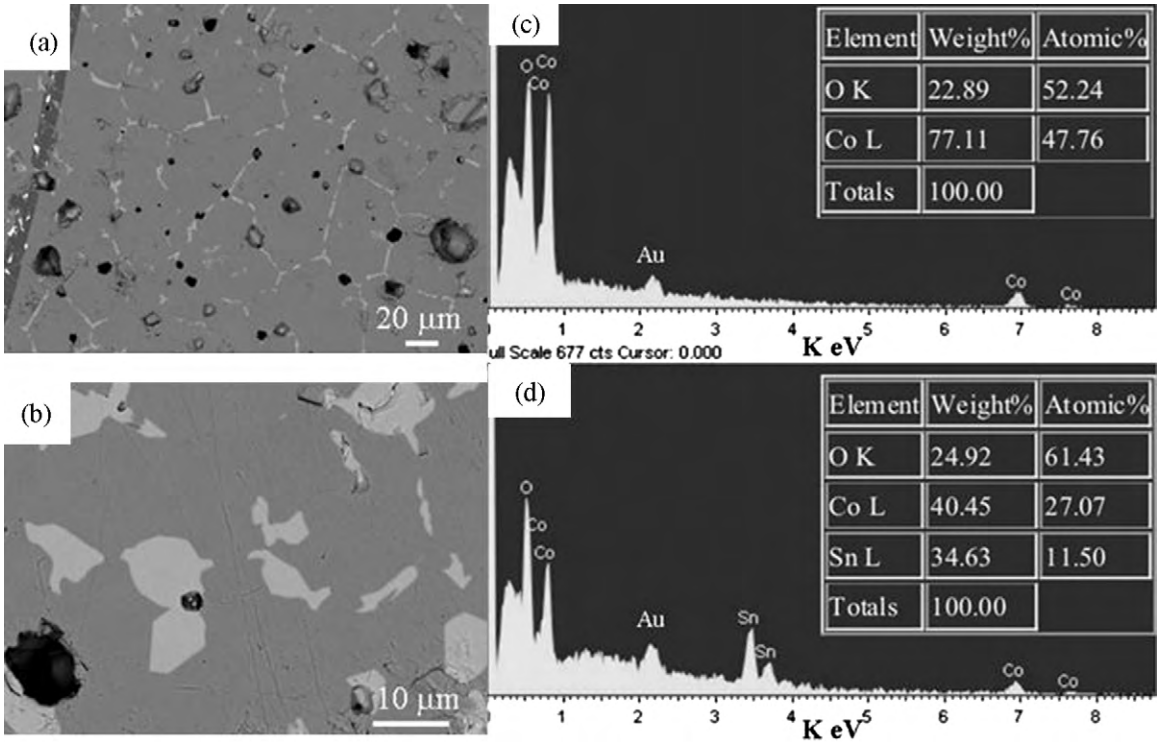

Fig. 2. (a) SEM BEI and (b) magnified view of the C92S8 sample reactively sintered at 1400 °C for 24 h and then cooled in furnace showing Sn^{4+}-doped $Co_{1-x}O$ matrix grains (dark) and intergranular $Co_{2+x}Sn_{1-x}O_4$ (bright), (c) and (d) point-count EDX spectra of the Sn^{4+}-doped $Co_{1-x}O$, and intergranular $Co_{2+x}Sn_{1-x}O_4$, respectively. The Au counts were due to sample coating.

3. Results

3.1. XRD

XRD indicated the C92S8 sample subject to sintering at 1400 °C and then furnace cooling contains abundant $Co_{2+x}Sn_{1-x}O_4$ spinel-type structure besides Sn^{4+}-doped $Co_{1-x}O$ of the rock salt-type structure (Fig. 1a). The C92S8 sample subject to sintering at 1400 °C and then air quenching is predominantly composed of Sn^{4+}-doped $Co_{1-x}O$ and rather minor $Co_{2+x}Sn_{1-x}O_4$ (Fig. 1b). Least-squares refinement of the *d*-spacings of both samples indicated the predominant phase of Sn^{4+}-doped $Co_{1-x}O$ to have a room-temperature lattice parameter $a = 0.4206 \pm 0.003$ nm, which is significantly smaller than the undoped value ($a = 0.4261$ according to JCPDS file 48-1719) indicating a considerable amount of Sn^{4+} dopant as discussed later. The lattice parameter determination of the spinel phase was not reliable because of biased

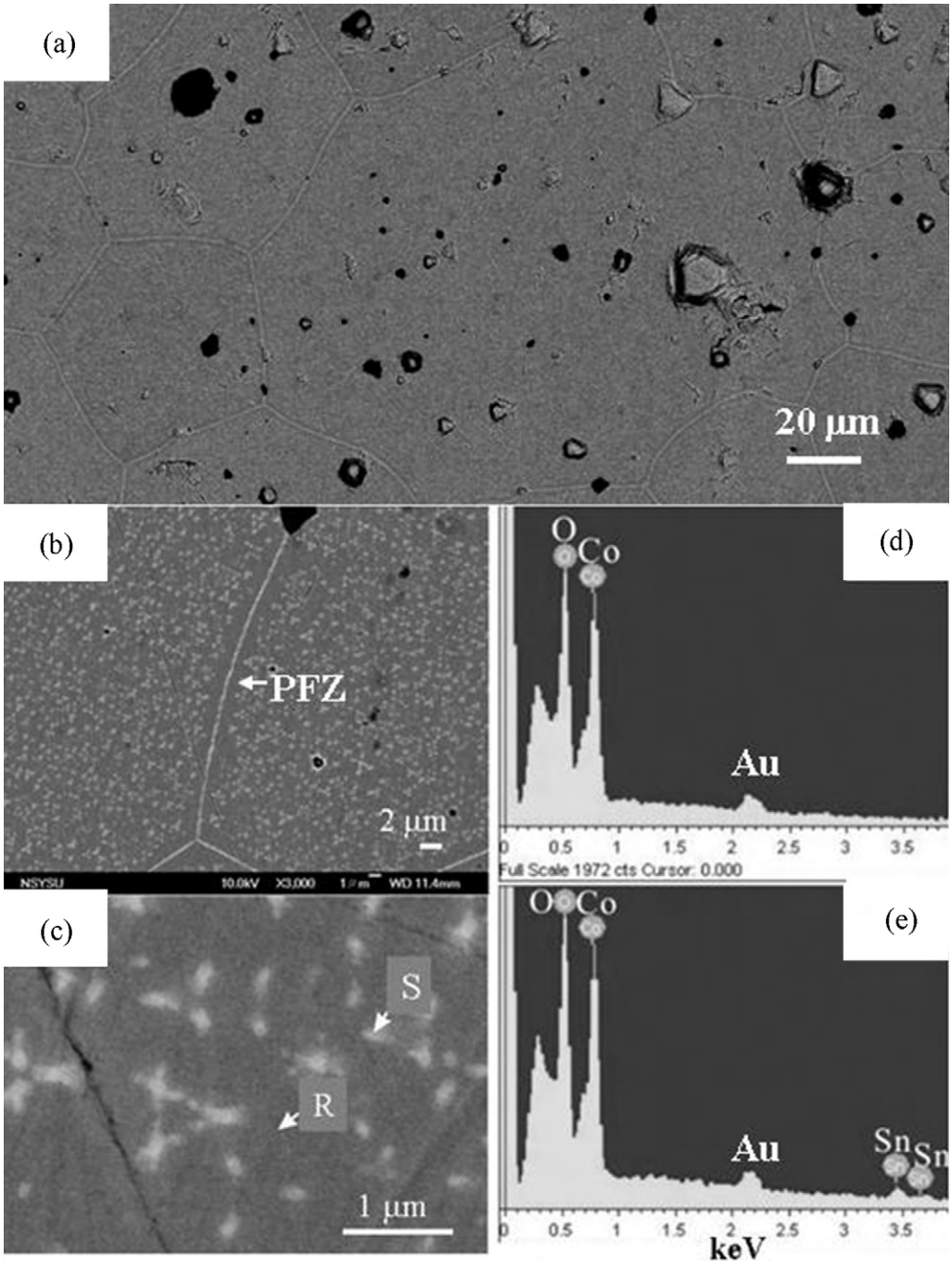

Fig. 3. SEM (a) SEI of C92S8 sample reactively sintered at 1400 °C for 200 h followed by air quenching, showing nonstoichiometric $Co_{2+x}Sn_{1-x}O_4$ phase was dispersed as intragranular particles and grain-boundary precipitates, (b) BEI and (c) further magnified BEI showing plate-like $Co_{2+x}Sn_{1-x}O_4$ spinel precipitates within the matrix grains of Sn^{4+}-doped $Co_{1-x}O$ and a precipitate free zone (PFZ) near the grain boundaries, (d) and (e) point-count EDX spectra taken from the matrix grain of Sn^{4+}-doped $Co_{1-x}O$ (denoted as R) and nonstoichiometric $Co_{2+x}Sn_{1-x}O_4$ spinel precipitates, respectively. The Au counts are due to sample coating for SEM observations.

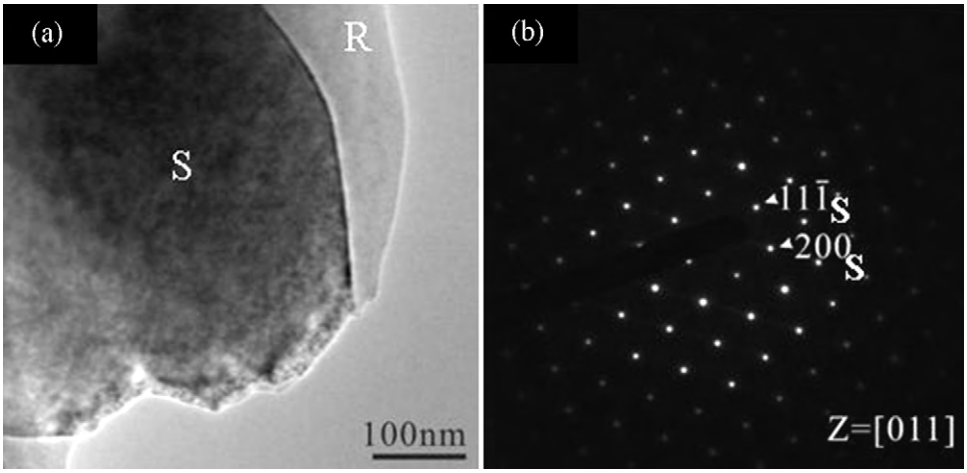

Fig. 4. TEM (a) BFI, (b) SAED pattern ([0 1 1] zone axis) of an intergranular $Co_{2+x}Sn_{1-x}O_4$ spinel (denoted as S) having no epitaxial relationship with the Sn^{4+}-doped $Co_{1-x}O$ (denoted as R) matrix. The C92S8 sample reactively sintered at 1400 °C for 24 h and then cooled in furnace.

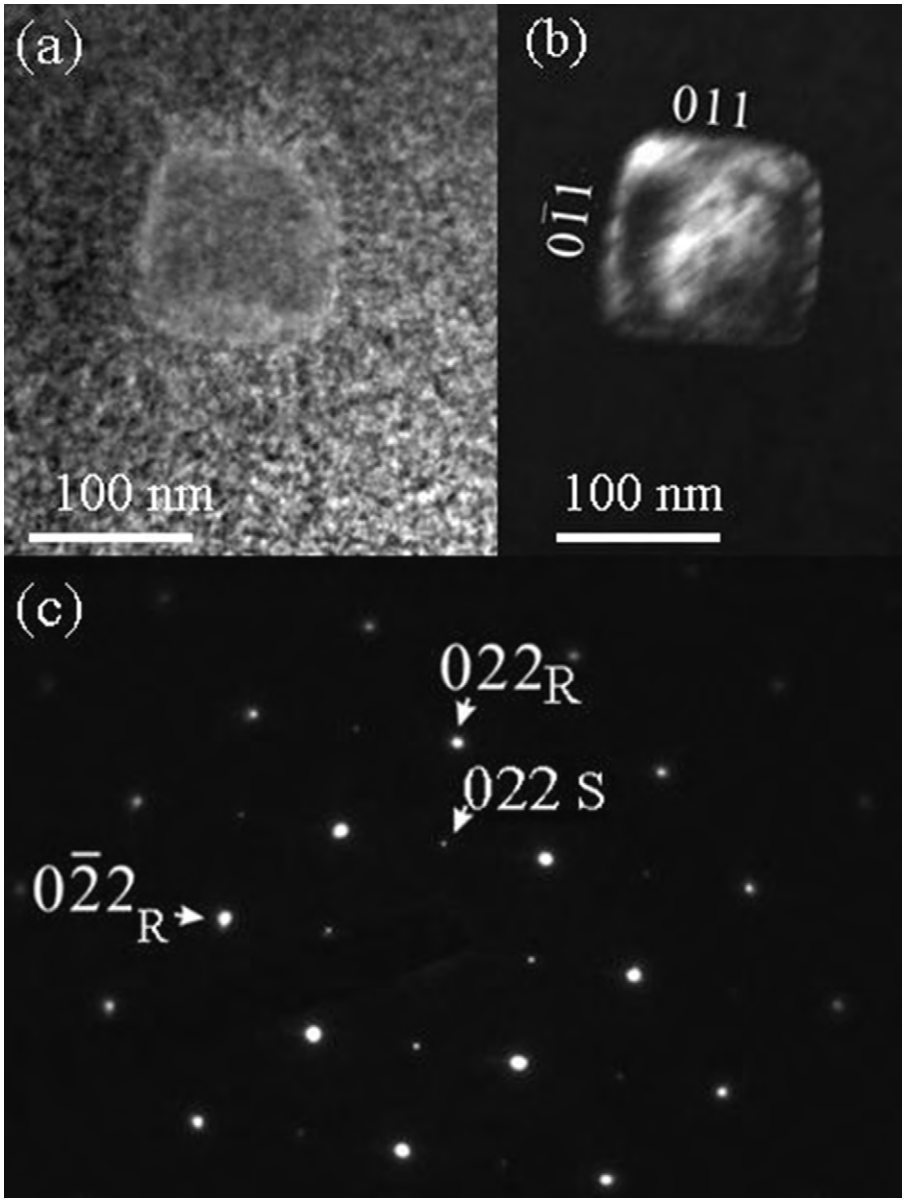

Fig. 5. TEM (a) BFI, (b) DFI using $(022)_S$ diffraction of the spinel and (c) SAED pattern of an octahedral $Co_{2+x}Sn_{1-x}O_4$ spinel nucleus which appears to be square in

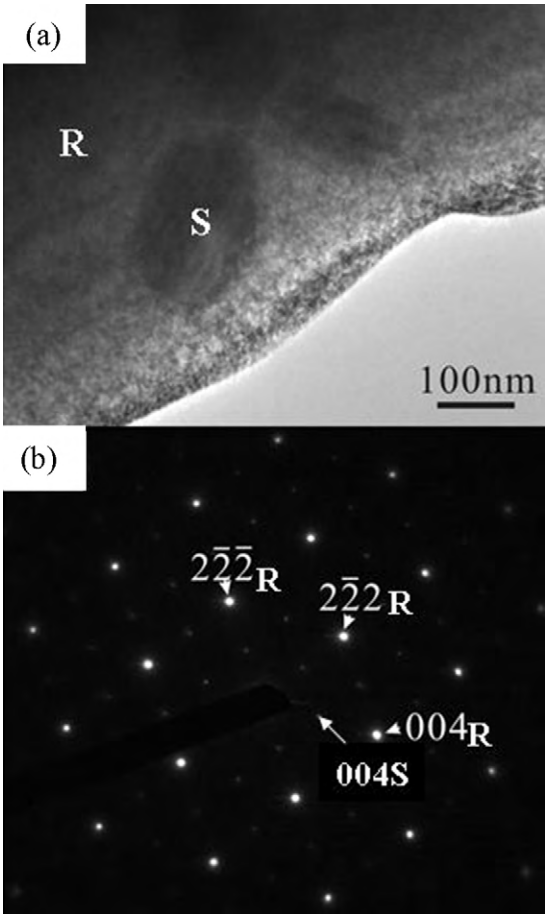

Fig. 6. TEM (a) BFI and (b) SAED pattern of the platy $Co_{2+x}Sn_{1-x}O_4$ spinel (S) precipitates in a matrix of Sn^{4+}-doped $Co_{1-x}O$ with rock salt-type structure (denoted as R) in [1 1 0] zone axis. The same specimen as in Fig. 5.

diffraction peaks due to inhomogeneous distribution of the intergranular spinel particles up to ca. 10 μm in size as indicated by SEM observations.

3.2. SEM

SEM BEI observations of the C92S8 sample reactively sintered at 1400 °C for 24 h and then cooled in furnace showed Sn^{4+}-doped $Co_{1-x}O$ matrix grains and $Co_{2+x}Sn_{1-x}O_4$ spinel which was dispersed as intergranular particles with equi-axed shape or precipitated at grain boundaries to have elongate shape as shown in Fig. 2a and further magnified in Fig. 2b. The compositions of the two phases were determined semi-quantitatively by point-count EDX analyses in Fig. 2c and d, respectively. Apparently, the intergranular spinel particles are primarily due to reactive sintering at 1400 °C whereas the secondary elongate spinels at grain boundaries are due to precipitation upon slow cooling from 1400 °C. It should be noted that the secondary spinel with bright contrast in the BEI (Fig. 2a and b) did not precipitate from the bulk nucleation sites of the Sn^{4+}-doped $Co_{1-x}O$ grains when slowly cooled in the furnace.

The C92S8 sample reactively sintered at 1400 °C for a longer time up to 200 h caused abnormal grain growth of Sn^{4+}-doped $Co_{1-x}O$ grains up to ca. 100 μm in size coupled with the detachment of the $Co_{2+x}Sn_{1-x}O_4$ particles and pores from the grain boundaries (Fig. 3a). Further magnified SEM images (Fig. 3b and c) showed the secondary $Co_{2+x}Sn_{1-x}O_4$ platelets which were precipitated not only at grain boundaries but also within Sn^{4+}-doped $Co_{1-x}O$ grains when the sample was quenched in air to trigger a cleaving-precipitation healing process as discussed later. A significant precipitate free zone (PFZ) ca. 2 μm in width was recognized near the grain boundaries of Sn^{4+}-doped $Co_{1-x}O$ (Fig. 3b). The chemical compositions of Sn^{4+}-doped $Co_{1-x}O$ matrix and the $Co_{2+x}Sn_{1-x}O_4$ precipitate were determined by point-count EDX analyses in Fig. 3d and e, respectively. It should be noted that the Sn counts were underestimated in Fig. 3e for the thin platy $Co_{2+x}Sn_{1-x}O_4$ precipitate because of additional counts contribution from the matrix grain of Sn^{4+}-doped $Co_{1-x}O$ due to electron beam broadening in the point-count EDX analysis.

3.3. TEM

TEM BFI and corresponding SAED pattern of the C92S8 sample reactively sintered at 1400 °C and then cooled in furnace showed typically the intergranular $Co_{2+x}Sn_{1-x}O_4$ spinel particle in [0 1 1] zone axis which has no epitaxial relationship with Sn^{4+}-doped $Co_{1-x}O$ matrix grains having the rock salt-type structure (Fig. 4).

By contrast the C92S8 sample reactively sintered at 1400 °C for 200 h and then air quenched showed additional $Co_{2+x}Sn_{1-x}O_4$ precipitates following parallel-epitaxial relationship with the matrix grain of Sn^{4+}-doped $Co_{1-x}O$ as shown by TEM images and corresponding SAED patterns (Figs. 5–7). The nanosize and isolated $Co_{2+x}Sn_{1-x}O_4$ precipitate tended to be octahedral in shape, i.e. appeared to be square with {1 1 1} habit planes in [1 0 0] zone axis (Fig. 5). The $Co_{2+x}Sn_{1-x}O_4$ precipitates however were platy when impinged as shown in [1 1 0] and [1 2 1] zone axes (Figs. 6 and 7, respectively). The platy precipitates were in fact preferentially distributed along the {0 1 1} planes, i.e. $(1\,0\,\bar{1})$ and $(0\,1\,\bar{1})$, of the host grain of Sn^{4+}-doped $Co_{1-x}O$ in [1 1 1] zone axis (Fig. 8). This implies a (*h k l*)-specific cleaving and precipitation healing process upon rapid quenching as discussed later. The $Co_{2+x}Sn_{1-x}O_4$ precipitate typically showed dislocations with half planes parallel to $\{0\,2\,\bar{2}\}$ as indicated by lattice image coupled with 2D Fourier transform in Fig. 8c and d, respectively. The modulated fringes near the $Co_{2+x}Sn_{1-x}O_4$ precipitates in the magnified BFI of Fig. 9a are Moiré fringes due the inclined {1 1 0} interfacial planes viewed in [1 1 4] zone axis. 2D forward and inverse Fourier transform (Fig. 9b and c, respectively) of the $Co_{2+x}Sn_{1-x}O_4$ lattice image in this zone axis (not shown) confirmed that its dislocation has a preferred half plane of

the matrix of Sn^{4+}-doped $Co_{1-x}O$ with rock salt-type structure (denoted as R) in [1 0 0] zone axis Sn^{4+}-doped $Co_{1-x}O$. C92S8 sample reactively sintered at 1400 °C for 200 h and then air quenched.

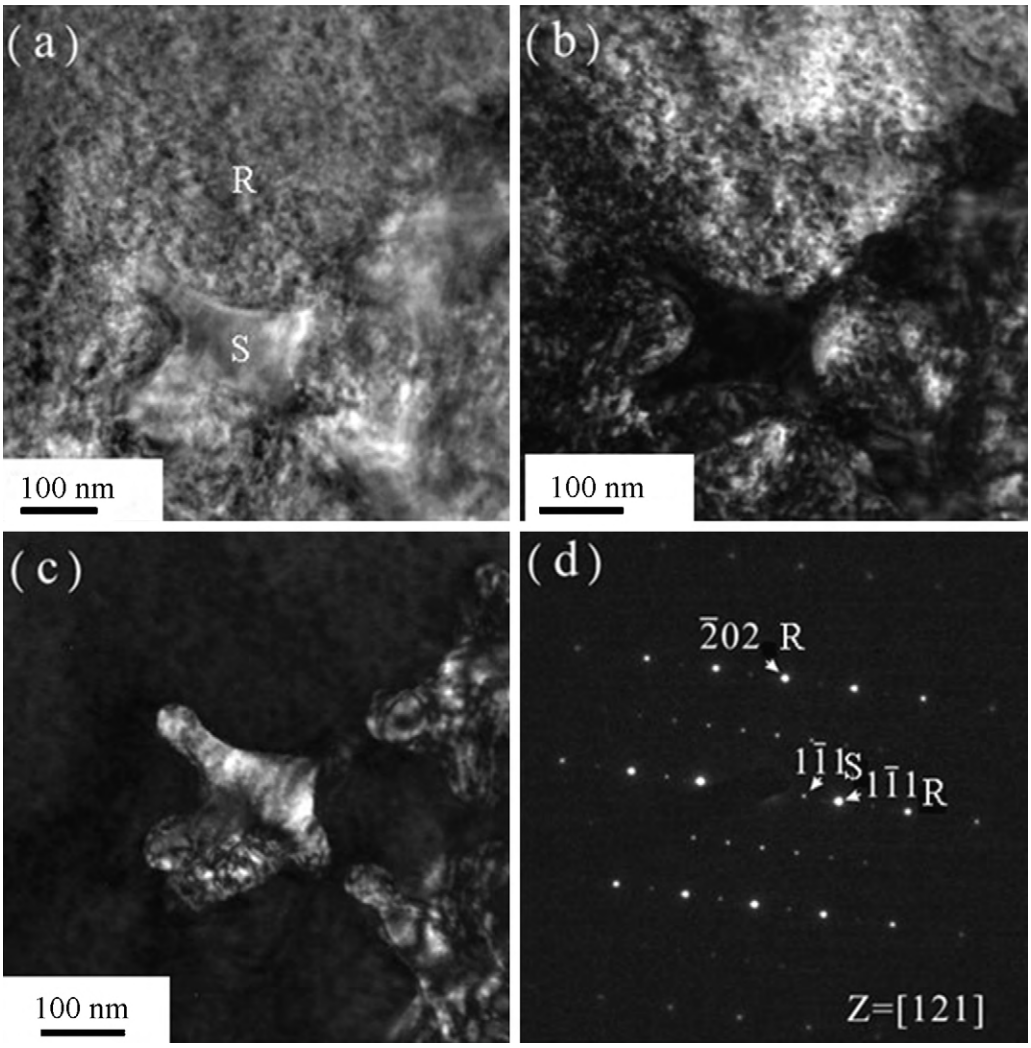

Fig. 7. TEM (a) BFI, (b) and (c) DFI using the (1 $\bar{1}$ 1) diffractions of rock salt-type Sn^{4+}-doped $Co_{1-x}O$ (denoted as R) and the $Co_{2+x}Sn_{1-x}O_4$ spinel precipitates (S), respectively, (d) SAED pattern in [1 2 1] zone axis. The same specimen as in Fig. 5.

$\{2\,\bar{2}\,0\}$. It should be noted that the paracrystalline distribution of point-defect clusters is vague in both Sn^{4+}-doped $Co_{1-x}O$ and $Co_{2+x}Sn_{1-x}O_4$ according to their SAED patterns showing no appreciable side-band diffraction spots.

4. Discussion

4.1. Defect chemistry of Sn^{4+}-doped $Co_{1-x}O$

The Sn^{4+} dopant in $Co_{1-x}O$ is expected to cause charge-compensating defect clusters $[V''_{Co} + Co_{Co}^{\bullet}]$ through the following equation in Kröger–Vink notation [17]:

$$SnO_2 \xrightarrow{CoO} Sn_{Co}^{\bullet\bullet} + 2[V''_{Co} + Co_{Co}^{\bullet}] + 2O_O^x \quad (1)$$

Here $Sn_{Co}^{\bullet\bullet}$ signifies dominating double positively charged tin at cobalt sites in the crystal lattice. A smaller X-ray lattice parameter for Sn-doped $Co_{1-x}O$ (0.4206 nm) than undoped $Co_{1-x}O$ (0.4260 nm) indicates that Sn^{4+} (effective ionic radii, 0.069 nm) replaced a larger sized Co^{2+} (0.0745 nm) for high spin rather than a smaller sized Co^{2+} (0.065 nm for low spin) in coordination number 6 [18]. It is also possible that the volume-compensating effect, due to the undersized Sn^{4+} dopant in the Co^{2+} site, forced $Co_{Co}^{\bullet}$ to enter the interstitial tetrahedral site, i.e. $Co_i^{\bullet\bullet\bullet}$, and hence more charge-compensating cation vacancies through the following equation:

$$Sn_{Co}^{\bullet\bullet} + [V''_{Co} + Co_{Co}^{\bullet}] \rightarrow Sn_{Co}^{\bullet\bullet} + [Co_i^{\bullet\bullet\bullet} + 4V''_{Co} + 4Co_{Co}^{\bullet}] \quad (2)$$

It cannot be excluded that smaller sized Co^{3+} (0.061 nm for high spin and 0.0545 nm for low spin state) than Co^{2+} (0.075 nm in high spin and 0.065 nm in low spin state) in octahedral sites [18] occurred upon cooling below 900 °C in air [19] to affect the defect chemistry of Sn^{4+}-doped $Co_{1-x}O$ in the present $Co_{1-x}O$–$Co_{2+x}Sn_{1-x}O_4$ composites. It also remains to be clarified whether the defect clustering scheme of Sn^{4+}-doped $Co_{1-x}O$ involves the 4:1 clusters; the 6:2 clusters composed of two 4:1 clusters with a common edge; and then a paracrystalline state, as the precursor of spinel phase, having cations ordered in

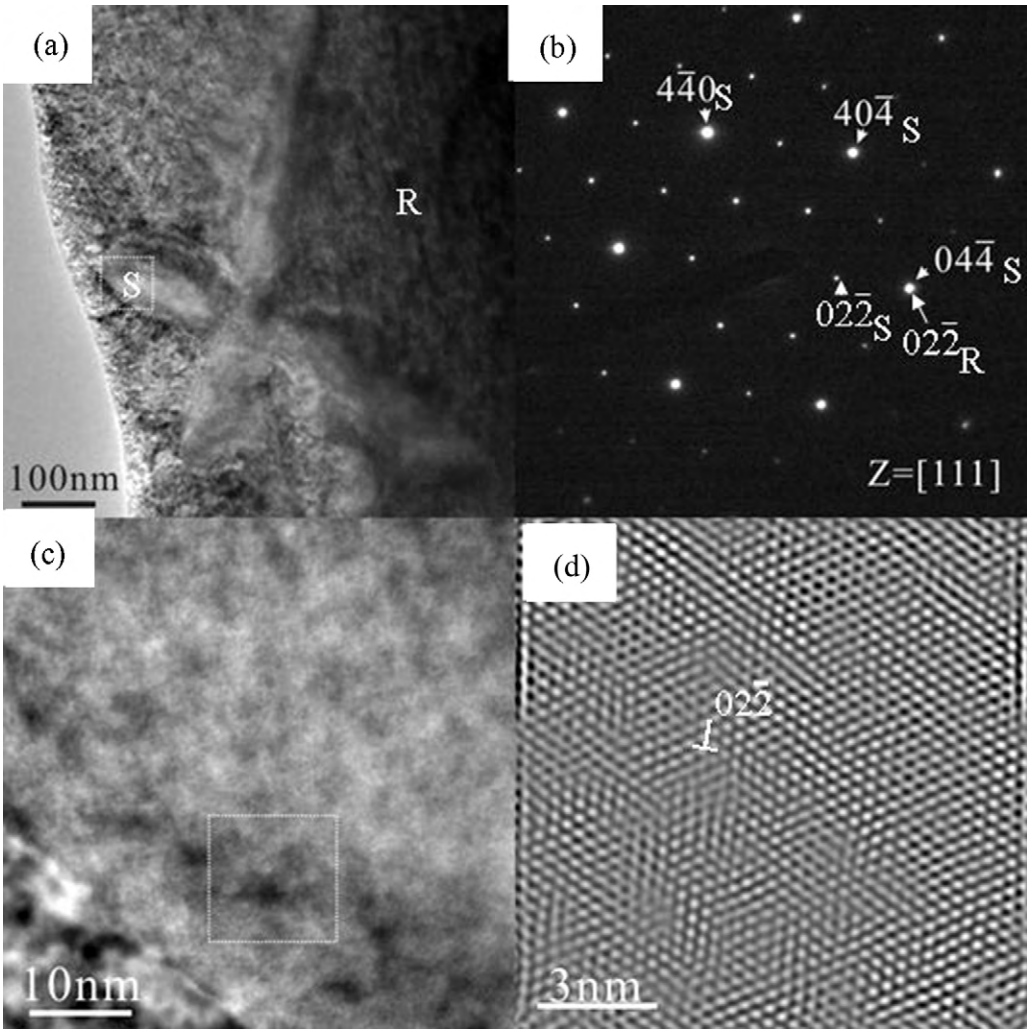

Fig. 8. TEM (a) BFI and (b) SAED pattern in [1 1 1] zone axis showing platy $Co_{2+x}Sn_{1-x}O_4$ spinel (S) precipitates with traces parallel to (1 0 $\bar{1}$) and (0 1 $\bar{1}$) of the rock salt-type host (R) of Sn^{4+}-doped $Co_{1-x}O$ in parallel-epitaxial relationship. (c) lattice image of the spinel magnified from the square region in (a), and (d) 2D Fourier transform of the square region in (c), showing dislocation (denoted by T) with half plane parallel to (0 2 $\bar{2}$). The same specimen as in Fig. 5.

the tetrahedral and octahedral sites, analogous to undoped nonstoichiometric iron oxide [5,6], cobalt oxide [20] and Zr^{4+}-doped $Co_{1-x}O$ [9].

4.2. Secondary spinel precipitation during slow cooling versus rapid quenching in air

The secondary $Co_{2+x}Sn_{1-x}O_4$ spinel was precipitated at the grain boundaries but not the bulk nucleation sites of Sn^{4+}-doped $Co_{1-x}O$ when slowly cooled in the furnace. The reasons for grain boundaries to act as the preferred precipitation sites are threefold. Firstly, high-angle grain boundary generally has low activation energy for heterogeneous nucleation [21]. Secondly, Sn segregation at grain boundaries as a result of high binding energy of solute [21] would facilitate the precipitation of Sn-rich phase, i.e. $Co_{2+x}Sn_{1-x}O_4$. Thirdly, grain boundary is generally a high-diffusivity path for a diffusional precipitation process [21].

By contrast, the secondary spinel was precipitated as parallel-epitaxial platelets within Sn^{4+} doped $Co_{1-x}O$ grains forming a PFZ near the grain boundary when air quenched. The platy spinel precipitation during rapid cooling in air can be rationalized by thermal-mismatch induced cleaving along specific crystallographic plane followed by a spontaneous healing/precipitation process. The linear thermal expansion coefficient of $Co_{1-x}O$ is 12–15 $\times 10^{-6}\,K^{-1}$ in the range of 300–1200 K according to experimental results [22] and semi-empirical estimation [23]. The Co-based spinel oxides, except $CoFe_2O_4$ with $12.1 \times 10^{-6}\,K^{-1}$, have a significantly lower thermal expansion coefficient of 7–9 $\times 10^{-6}\,K^{-1}$ at 800 °C [24]. Thus, the thermal-mismatch between the Sn^{4+}-doped $Co_{1-x}O$ grains and primarily dispersed $Co_{2+x}Sn_{1-x}O_4$ particles is large enough upon rapid cooling through 800 °C to cause microcracks taking advantage of cobalt vacancies and their associated defect clusters as mentioned. The microcracks were predominantly formed as microcleavages parallel to the {1 1 0} planes of $Co_{1-x}O$ because of its relatively low shear modulus (c' = 571 kb) than {1 0 0} (c_{44} = 830 kb) [12,25] and less breaking of periodic bond chains [26] than the most close packed {1 1 1} planes. The {1 1 0} cleavages could be oxidized

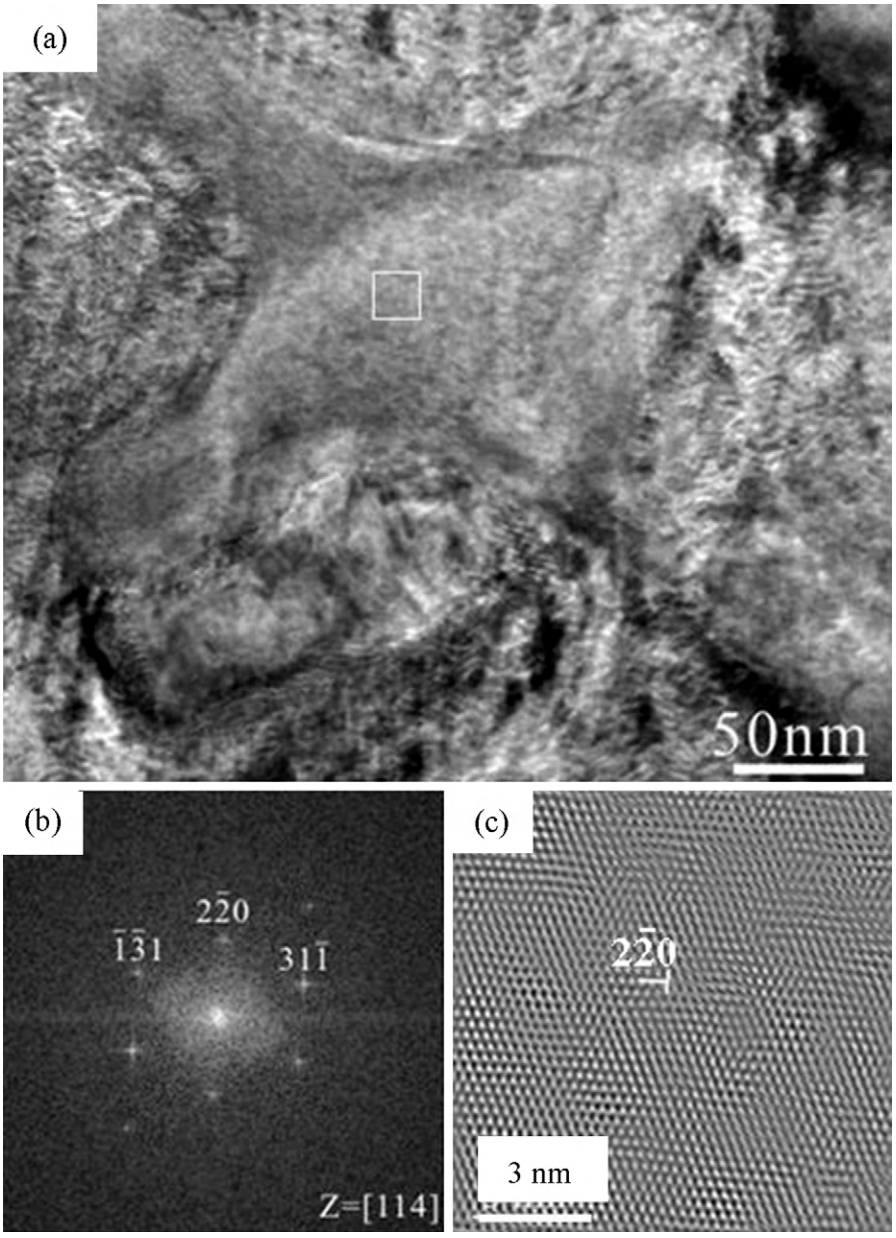

Fig. 9. TEM (a) BFI of the $Co_{2+x}Sn_{1-x}O_4$ spinel precipitates and rock salt-type host with parallel-epitaxial relationship to illustrate Moiré fringes, (b) and (c) 2D forward and inverse Fourier transform of the $Co_{2+x}Sn_{1-x}O_4$ lattice image take from the square region in (a) showing dislocation (denoted by T) with half plane parallel to (2 $\bar{2}$ 0) as viewed edge on in [1 1 4] zone axis. The same specimen as in Fig. 5.

to form $Co_{3-\delta}O_4$ spinel below 900 °C in air [19]. However, the accompanied segregation of Sn^{4+} dopant to the {1 1 0} cleavages during cooling would prefer the precipitation of $Co_{2+x}Sn_{1-x}O_4$ spinel with varied stoichiometries. Such a {*h k l*}-specific cleaving and spontaneous healing-precipitation process is analogous to thermal-mismatch induced {1 1 0} cleaving and spontaneous healing of zirconia dispersed $Co_{1-x}O$ [12] and transformation-enabled cleaving and healing in zirconia dispersed $Co_{1-x}O$ [13]. As for the PFZ, it can be attributed to the depletion of bulk nucleation sites, i.e. site saturation of cobalt vacancies and their associated defect clusters near the grain boundary, during rapid cooling analogous to the case of PFZ formation in an Al–Ge alloy [27].

4.3. Formation of spinel embryo with stable habit plane

The $Co_{2+x}Sn_{1-x}O_4$ spinel nanocrystals just nucleated from cobalt vacancies and/or defect clusters with rather limited extent of growth upon rapid cooling showed well-developed {1 1 1} habit plane. By contrast, in our previous study of MgO/Mg_2TiO_4 composite, nanosize precipitates of Mg_2TiO_4 spinel were found to precipitate from Guinier–Preston (G.P.) zones [21] in Ti-doped MgO upon cooling [28]. The nucleation of spinel phase rather than metastable G.P. zone is common for nonstoichiometric transition metal oxides of rock salt-type structure such as wustite $Fe_{1-x}O$ [5,6], $Ni_{1-x}O$ dissolved with Zr^{4+} [7] or Ca^{2+} [8], and $Co_{1-x}O$ dissolved with Zr^{4+} [9] or

Mg^{2+} [10]. However, the paracrystalline distribution of 4:1 defect clusters is vague in Sn^{4+}-doped $Co_{1-x}O$ in comparison with the significant paracrystals in $Co_{1-x}O$ dissolved with Zr^{4+} [9] or Mg^{2+} [10]. Apparently, the driving force to precipitate directly the $Co_{2+x}Sn_{1-x}O_4$ spinel is strong enough to bypass the metastable formation of G.P. zones and paracrystals in Sn^{4+}-doped $Co_{1-x}O$ upon exsolution.

The {1 1 1} habit-plane selection of parallel-epitaxial spinel could have something to do with the coherency strain energy minimization across the interface of Sn-doped $Co_{1-x}O$ and its $2 \times 2 \times 2$ superlattice, i.e. the $Co_{2+x}Sn_{1-x}O_4$ spinel nanocrystal. In this connection, very small $NiFe_2O_4$ particles between 1 and 4 nm in size have been observed in an Fe-doped NiO sample quenched during early stages of spinel precipitation [16]. The critical size for $NiFe_2O_4$ spinel nucleation was estimated to be 4.3 nm and the embryos were also found to be bounded by <1 1 1> planes with an octahedral morphology for a minimum energy. The grown spinel plate however has {1 0 0} habit plane as for $NiFe_2O_4$ in NiO [15] or {1 1 0} habit plane as for $Co_{2+x}Sn_{1-x}O_4$ in $Co_{1-x}O$ under the influence of a $\{h\,k\,l\}$-specific cleaving and spontaneous healing/precipitation event.

5. Conclusions

1. Secondary $Co_{2+x}Sn_{1-x}O_4$ spinels were precipitated at grain boundaries of Sn^{4+} doped $Co_{1-x}O$ when the $Co_{1-x}O$–$Co_{2+x}Sn_{1-x}O_4$ composite was slowly cooled from 1400 °C.
2. The $Co_{2+x}Sn_{1-x}O_4$ spinels occurred as parallel-epitaxial platelets within Sn^{4+} doped $Co_{1-x}O$ grains forming a precipitate free zone near the grain boundaries when the $Co_{1-x}O$–$Co_{2+x}Sn_{1-x}O_4$ composite was air quenched from 1400 °C.
3. Thermal-mismatch induced {1 1 0} cleaving taking advantage of cobalt vacancies and spontaneous healing by oxidation and segregation account for the platy spinel precipitation within the grains. The precipitate free zone can be attributed to cobalt vacancy and/or defect cluster depletion, i.e. site saturation, near the grain boundaries during rapid cooling in air.
4. The spinel nanocrystals nucleated from cobalt vacancy and its associated defect clusters have well-developed {1 1 1} habit plane in order to minimize the coherency strain energy.

Acknowledgements

Supported by the Center for Nanoscience and Nanotechnology of NSYSU and partly by National Science Council, Taiwan ROC. We thank Mr. Bo-Cheng Lin for the help on the analysis of some TEM images.

References

[1] T.R. Welberry, A.G. Christy, A paracrystalline distribution of defect distributions in wüstite, $Fe_{1-x}O$, J. Solid State Chem. 117 (1995) 398–406.
[2] T.R. Welberry, A.G. Christy, Defect distribution and the diffuse X-ray diffraction pattern of wüstite, $Fe_{1-x}O$, Phys. Chem. Miner. 24 (1997) 24–38.
[3] B.E.F. Fender, F.D. Riley, in: L. Eyring, M. O'Keefe (Eds.), The Chemistry of Extended Defects in Non-Metallic Solids, North-Holland, Amsterdam, 1970.
[4] C.R.A. Catlow, B.E.F. Fender, Calculation of defect clustering in $Fe_{1-x}O$, J. Phys. C: Solid State Phys. 8 (1975) 3267–3279.
[5] P. Vallet, P. Raccah, On the studies of thermodynamic properties of ferrous oxides, Mem. Sci. Rev. Metall. 62 (1965) 1–29.
[6] B. Andersson, J.O. Sletnes, Decomposition and ordering in $Fe_{1-x}O$, Acta Crystallogr. Sect. A 33 (1977) 268–276.
[7] J. Chen, P. Shen, Defect clusters and superstructure of Zr^{4+}-dissolved $Ni_{1-x}O$, J. Solid State Chem. 140 (1998) 361–370.
[8] M.L. Jeng, P. Shen, Paracrystal formation from $Ni_{1-x}O$ and CaO upon interdiffusion, J. Solid State Chem. 152 (2000) 421–427.
[9] K.T. Lin, P. Shen, Interdiffusion-induced phase changes of $Co_{1-x}O$/zirconia composites, J. Solid State Chem. 145 (1999) 739–750.
[10] T.M. Tsai, K.C. Yang, P. Shen, Defect clusters and precipitation/oxidation of MgO–$Co_{1-x}O$ solid solution, J. Solid State Chem. 177 (2004) 3301–3309.
[11] P. Shen, J.Y. Wang, Cellular paracrystal formation from Co-doped CaO polycrystals, J. Solid State Chem. 161 (2001) 341–347.
[12] W.H. Lee, P. Shen, Thermal-mismatch induced cleaving and spontaneous healing of zirconia dispersed $Co_{1-x}O$, Mater. Sci. Eng. A 332 (2002) 262–269.
[13] M.Y. Li, P. Shen, S.L. Hwang, Transformation-enabled cleaving and healing in zirconia dispersed $Co_{1-x}O$, Mater. Sci. Eng. A 386 (2004) 104–111.
[14] S.L. Hwang, T.F. Yui, H.T. Chu, P. Shen, H.P. Schertl, R.Y. Zhang, J.G. Liou, On the origin of oriented rutile needles in garnet from UHP eclogites, J. Metamorph. Geol. 25 (2007) 349–362.
[15] K.M. Ostyn, C.B. Carter, M. Koehne, H. Falke, H. Schmalzried, Internal reactions in oxide solid-solutions, J. Am. Ceram. Soc. 67 (1984) 679–685.
[16] S.R. Summerfelt, C.B. Carter, Direct observation of nucleation embryos during $NiFe_2O_4$ precipitation in NiO, J. Mater. Res. 7 (1992) 1271–1277.
[17] F.A. Kröger, H.J. Vink, Relations between the concentrations of imperfections in crystalline solids, Solid State Phys. 3 (1956) 307–435.
[18] R.D. Shannon, Revised effective ionic radii and systematic studies of interatomic distances in halides and chalcogenides, Acta Crystallogr. A 32 (1976) 751–767.
[19] M. Oku, Y. Sato, In-situ X-ray photoelectron spectroscopic study of the reversible phase transition between CoO and Co_3O_4 in oxygen of 10^{-3} Pa, Appl. Surf. Sci. 55 (1992) 37–41.
[20] W.H. Lee, P. Shen, $Co_{3-\delta}O_4$ paracrystal: 3-D assembly of nano-size defect clusters in spinel lattice, J. Solid State Chem. 177 (2004) 101–108.
[21] D.A. Porter, K.E. Easterling, M.Y. Sherif, Phase Transformations in Metals and Alloys, 3rd edition, CRC Press, Boca Raton, 2009.
[22] Y.S. Touloukian, R.K. Kibby, R.E. Taylor, T.Y.R. Lee, Thermophysical Properties of Matter Thermal Expansion of Nonmetallic Solids, vol. 13, Plenum, New York, 1970.
[23] H. Inaba, Semi-empirical estimation of thermal expansion coefficients of oxides, Jpn. J. Apply. Phys. 35 (1996) 4730–4735.
[24] A. Petric, H. Ling, Electrical conductivity and thermal expansion of spinels at elevated temperatures, J. Am. Ceram. Soc. 90 (2007) 1515–1520.
[25] J.P. Poirier, Introduction to Physics of the Earth's Interior, Cambridge University Press, Cambridge, 1991, p. 15.
[26] P. Hartman, W.G. Perdok, On the relations between structure and morphology of crystals. I, Acta Crystallogr. 8 (1955) 49–52.
[27] G. Lorimer, Precipitation in Solids, The Metallurgical Society of AIME, Warrendale, PA, 1978.
[28] K.C. Yang, P. Shen, On the precipitation of coherent spinel nanoparticles in Ti-doped MgO, J. Solid State Chem. 178 (2005) 661–670.